

Computational explorations of a deformed fuzzy sphere

L Glaser ^{*1}

¹University of Vienna, Faculty of Physics, Boltzmanngasse 5,
1090 Vienna, Austria

12th December 2023

Abstract

This work examines the deformed fuzzy sphere, as an example of a fuzzy space that can be described through a spectral triple, using computer visualizations. We first explore this geometry using an analytic expression for the eigenvalues to examine the spectral dimension and volume of the geometry. In the second part of the paper we extend the code from L. Glaser and A. B. Stern. In: *Journal of Geometry and Physics* 159 (2021), in which the truncated sphere was visualized through localized states. This generalization allows us to examine finite spectral triples. In particular, we apply this code to the deformed fuzzy sphere as a first step in the more ambitious program of using it to examine arbitrary finite spectral triples, like those generated from random fuzzy spaces, as show in J. W. Barrett and L. Glaser. In: *J.Phys.* A49 (May 2016).

1 Introduction

Quantizing gravity is one of the most difficult open questions remaining in fundamental physics. One way to approach this problem is to closer examine

*L.glaser@univie.ac.at

the mathematical structure underlying our theories, to rewrite them in a more elegant way. Recasting the differential geometry of a manifold as the algebraic data of a spectral triple is one such way. Writing geometry in an algebraic language like this is promising since many of quantum theory's unintuitive results arise from its underlying algebraic structure.

A spectral triple consists of an algebra, a Hilbert space and a Dirac operator $(\mathcal{A}, \mathcal{H}, D)$. Any compact Riemannian manifold can be described as a commutative spectral triple which fulfils a number of axioms, as proposed by Connes in [3]. He showed in particular that the metric information of the manifold can be recovered using the distance between pure states s_1, s_2 of the algebra, defined as

$$d(s_1, s_2) = \sup_{a \in \mathcal{A}} \left\{ |s_1(a) - s_2(a)| \mid |[D, a]| \leq 1 \right\} . \quad (1)$$

In this article we will be studying real finite spectral triples as defined by John Barrett in [4]. A real spectral triple $(s, \mathcal{A}, \mathcal{H}, D, J, \Gamma)$ arises when describing a spin manifold. In addition to the algebra, Hilbert space and Dirac operator it has a KO-dimension s , a real structure J and a chirality Γ . The spectral triples we examine are a subclass called matrix geometries in [4]. For these the algebra consists of n by n matrices $\mathcal{A} = M_n(\mathbb{C})$, and the Hilbert space is a product space $\mathcal{H} = V \otimes M_n(\mathbb{C})$, with V a (p, q) -Clifford module. The (p, q) -Clifford module is generated by q γ -matrices with $\gamma_i^2 = -1$ and p γ -matrices with $\gamma_i^2 = 1$. The KO-dimension is then given as $s = q - p \pmod{8}$. The algebra acts on the Hilbert space through a representation $\rho(a)$ with $\rho(a)(v \otimes m) = v \otimes a \cdot m$ where $m, a \in M_n(\mathbb{C})$ with $a \cdot m$ the usual matrix product and $v \in V$. The real structure J connects the left action of the algebra on the Hilbert space to the right action as $\rho_l(a) = J\rho_r(a)J^{-1}$. The Dirac operator on such a spectral triple has to fulfil a number of conditions; it should be self adjoint, commute or anti-commute with J and Γ depending on the KO-dimension, and satisfy the first order condition

$$[[D, \rho_r(a)], \rho_l(b)] = 0 \quad \forall \quad a, b \in \mathcal{A} .$$

Taking all of these conditions on the Dirac operator into account leads to a restricted parametrization of the Dirac operator, purely through a set of hermitian and anti-hermitian matrices in $M_n(\mathbb{C})$

$$D(v \otimes m) = \sum_i \omega_i v \otimes (K_i m + \epsilon' K_i^*) \quad (2)$$

where ω_i are products of γ matrices and K_i are matrices that are hermitian or anti-hermitian respectively, depending on the sign ϵ' and whether the product ω_i is hermitian or anti-hermitian (more detail on this is given in [4]).

This parametrization becomes immediately obvious if we look at the well known Grosse-Presnăjder Dirac operator for the fuzzy sphere

$$D_{GP}(v \otimes m) = v \otimes m + \sum_{j < k} \sigma^j \sigma^k v \otimes [L_{jk}, m] , \quad (3)$$

where σ^j are the Pauli matrices and L_{jk} are the generators of the Lie algebra $so(3)$ in an n -dimensional irreducible representation on \mathcal{H} . This operator acts on a Hilbert space with a $(0, 3)$ -Clifford module, leading to KO-dimension $s = 3$, while the sphere has KO-dimension $s = 2$. It also leads to a non-symmetric spectrum, since the largest eigenvalue of the operator has no corresponding negative eigenvalue. These points led Barrett to propose an alternative Dirac operator for the fuzzy sphere, acting on a $(1, 3)$ -Clifford module

$$D_{S^2}(v \otimes m) = \gamma^0 v \otimes m + \sum_{j < k} \gamma^0 \gamma^j \gamma^k v \otimes [L_{jk}, m] , \quad (4)$$

where now the γ^j are $(1, 3)$ -Clifford matrices and $(\gamma^0)^2 = 1$. This operator consists of two copies of the Grosse-Presnăjder operator, acting on the ± 1 subspaces of the matrix γ^0 .

Parametrizing the Dirac operator through a set of matrices has opened the door to defining an ensemble of finite spectral triples [2, 5]. The premise of this work was, that finite spectral triples as defined above are a generalization of discrete geometries, which certainly includes well known cases like the fuzzy sphere. Thus fixing the algebra and Hilbert space, while varying the Dirac operator over all operators parametrized as in equation (2) would create an ensemble of geometric and not so geometric spectral triples

$$\mathcal{Z} = \int \mathcal{D}[D] e^{-\mathcal{S}(D)} . \quad (5)$$

Using the Haar measure on the space of matrices K_i and defining some spectral action $\mathcal{S}(D) = Tr(f(D))$ does then allow us to define this path integral over finite spectral triples, as a multi matrix model

$$\mathcal{Z} = \int \mathcal{D}[K_i] e^{-\mathcal{S}(K_i)} . \quad (6)$$

This may be studied using computer simulations, as e.g. done in [2, 6, 5, 7] or using analytic techniques [8, 9, 10, 11, 12, 13, 14]. The action used for these studies was a simple quartic action $\mathcal{S}(D) = \text{Tr}(D^4) + g_2 \text{Tr}(D^2)$, with a single coupling constant g_2 . Exploring a range of possible values of (p, q) and searching for a phase transition in g_2 showed that even this simple model has a rich structure. A closer look at spectral observables, like the dimension, then indicated that the model has the potential to dynamically favour geometric spectral triples, in particular at phase transition points [6, 5].

These results lead to the question: are there any more tools to understand whether a finite spectral triple is associated to a geometry, and if it is, how the associated geometry looks? A partial answer, from a slightly different context came in [1] where we developed an algorithm to visualize truncated spectral triples. In the present article we will explore an extension of this code, towards visualizations of finite spectral triples, to try and recover their geometry. The first step in this process is to visualize, and thus better understand, one particular class of finite spectral triples, which are the deformed fuzzy sphere.

This paper is split into five parts, starting with this introduction. The second section then introduces the deformed fuzzy sphere, and studies its eigenvalues and some geometric properties which can be derived from these. The third section describes the code used to visualize the deformed fuzzy sphere, with a particular focus on those parts of the code that were modified compared to past work. In the fourth section we will analyse the visualizations of the deformed fuzzy sphere, and explain the images we find. The last section consists of a conclusion and outlook, pointing towards possible further applications of this algorithm, and gaps within this work that might be usefully filled.

2 The spectrum of a deformed fuzzy sphere

An interesting modification of the fuzzy sphere, given in (4), is the deformed fuzzy sphere, in which the Dirac operator is changed to be

$$D(v \otimes m) = c_0 \gamma^0 v \otimes m + \sum_{j < k=1}^3 c_{jk} \gamma^0 \gamma^j \gamma^k v \otimes [L_{jk}, m] \quad (7)$$

where $c_0, c_{jk} \in \mathbb{R}$ are deformation parameters. If we restrict this most general extension to only introduce two parameters a, c

$$D(v \otimes m) = a\gamma^0 v \otimes m + c\gamma^0\gamma^1\gamma^2 v \otimes [L_{12}, m] + \gamma^0\gamma^1\gamma^3 v \otimes [L_{13}, m] + \gamma^0\gamma^2\gamma^3 v \otimes [L_{23}, m], \quad (8)$$

we are able to find exact analytic results for the eigenvalues, very similar to how it is done for the ordinary fuzzy sphere. The derivation of these eigenvalues, and a closer analytic study of the classical analogue of this operator will be published in future work [15]. The analytic expression for the eigenvalues comes out as

$$\lambda_{j,k} = \pm \left(a - \frac{c}{2} + \sqrt{j^2 + (c^2 - 1)k^2} \right) \quad (9)$$

$$\text{for } j = \frac{1}{2}, \frac{3}{2}, \dots, n - \frac{1}{2} \quad k = \frac{1}{2}, \frac{3}{2}, \dots, j \quad (10)$$

$$\lambda_{j,k} = \pm \left(a - \frac{c}{2} - \sqrt{(j+1)^2 + (c^2 - 1)k^2} \right) \quad (11)$$

$$\text{for } j = \frac{1}{2}, \frac{3}{2}, \dots, n - \frac{3}{2} \quad k = \frac{1}{2}, \frac{3}{2}, \dots, j. \quad (12)$$

Each of these eigenvalues arises with multiplicity two, giving us a symmetric, real spectrum of eigenvalues for the deformed fuzzy sphere. This spectrum, for $n = 20$ is shown in Figure 1.

In the left-hand picture we look at $c \geq 1$, there we see that as the deformation becomes stronger the maximal eigenvalue increases and the spectrum flattens out. The central region still shows a linear rise, however this region becomes smaller as the deformation becomes stronger.

The right-hand image shows $0 \leq c \leq 1$, and we can see that in this region the influence of the deformation is not as strong, although for $c = 0$ eigenvalues of value 0 appear.

Using these results we can examine spectral observables for the deformed fuzzy sphere. Two particularly interesting cases of this, which we will use in the visualization algorithm to decide how many coherent states to generate for each geometry, are the spectral dimension and the volume of the geometry.

Before we examine these we would like to understand what effect the deformation has on the shape of the geometry. To study this we examine the continuum equation for an ellipsoid

$$r^2 = \frac{x_1^2}{\alpha^2} + \frac{x_2^2}{\beta^2} + \frac{x_3^2}{\gamma^2}, \quad (13)$$

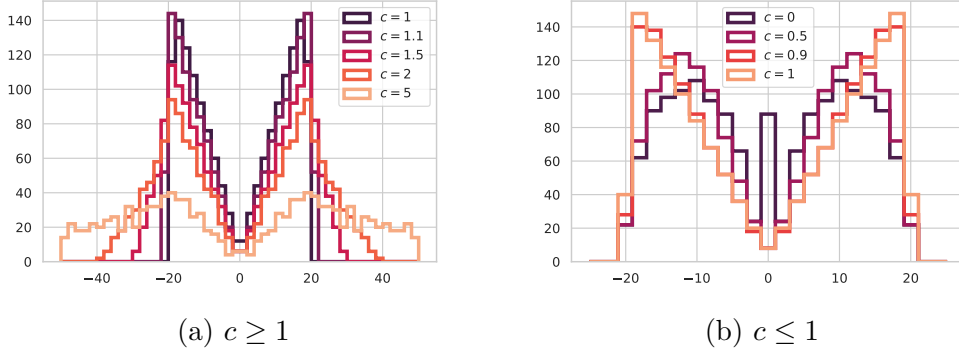


Figure 1: Histogram of the eigenvalue spectrum for $n = 20$ for a range of deformation parameters

and compare it to a continuum deformed Dirac operator

$$D_{cont} = (\sigma \cdot x) \sum_{i < j} c_{ij} \sigma^i \sigma^j \nabla_{X_{ij}} \quad (14)$$

where the vector fields for the sphere are $X_{ij} = x^i \partial_{x^j} - x^j \partial_{x^i}$. To see how α, β, γ relate to the c_{ij} we evaluate the continuum Dirac at special points, e.g. for $x = (0, 0, 1)$ the Dirac becomes

$$D_{cont(0,0,1)} = c_{13} \sigma^1 \partial_{x^1} + c_{23} \sigma^2 \partial_{x^2} . \quad (15)$$

For general c_{ij} this operator is not symmetric along the two directions x^1, x^2 . However, if we rescaled a continuum ellipsoid as $x^1 \rightarrow x^1/\alpha, x^2 \rightarrow x^2/\beta, x^3 \rightarrow x^3/\gamma$ then the rescaling would lead to new coordinates in which the ellipsoid is a sphere. So if we do this rescaling we find that $c_{13}\alpha$ and $c_{23}\beta$ should be the same, to lead to a symmetric operator in equation (15). This gives us a relation between α, β and c_{12}, c_{23} . Repeating this for the points $(1, 0, 0)$ and $(0, 1, 0)$ we find two more similar relations. Using these we can, up to an overall prefactor, understand the relation between the axes lengths of the ellipse and the deformation parameters in our Dirac operator

$$\alpha = \frac{1}{c_{12}c_{13}} \quad \beta = \frac{1}{c_{12}c_{23}} \quad \gamma = \frac{1}{c_{13}c_{23}} . \quad (16)$$

This discussion has avoided considering the additional terms in the Dirac arising from the connection in the covariant derivative. However since the derivative terms definitely have to scale correctly this treatment is sufficient to fix the scaling.

2.1 Spectral dimension

Based on our understanding about the shape of the geometry we can then study spectral observables. We begin with the spectral dimension, which was first studied in causal dynamical triangulations [16]. It is a dimension measure that can resolve how the dimension of a geometry behaves with scale. As a simple example, a 2-sphere is 2-dimensional if we are looking at length scales smaller than the radius of the sphere, but appears like a point if we are observing scales that are much larger than the radius. A dimension spectrum like this is particularly interesting for quantum geometries, since their quantum structure can give rise to changes in dimension at small scales.

The prototypical example of this is in 4 dimensional causal dynamical triangulations which find a UV scale dimension close to 2, while at larger scales it recovers the expected 4 dimensional behaviour before dropping to 0 for low energies [16]. For fuzzy spaces the spectral dimension is defined from the eigenvalues of the Dirac operator $\{\lambda\}$ as

$$d_s(t) = 2t \langle \lambda^2 \rangle = 2t \frac{\sum_{\lambda} \lambda^2 e^{-t\lambda^2}}{\sum_{\lambda} e^{-t\lambda^2}} . \quad (17)$$

This expression runs into a problem for geometries with a non-zero lowest energy mode, since this will dominate the expression at large t and thus hide the large scale structure.

The Dirac operators for fuzzy spaces often have a non-zero smallest eigenvalue, so in [6] we introduced the spectral variance. Our studies showed that this new observable works similar to the spectral dimension, but can also usefully be studied for operators that do not have a zero mode

$$v_s(t) = 2t^2 \left(\langle \lambda^4 \rangle - \langle \lambda^2 \rangle^2 \right) . \quad (18)$$

Calculating this using the spectra for $n = 20$ from above we find Figure 2. There we see that, for the deformations with $c > 1$ the geometry seems to be approximately 2 dimensional on short scales, but then appears 1 dimensional on large scales. This is consistent with a sphere being narrowed down to a cigar shape, as our scaling analysis above predicts. The behaviour for $c < 1$ is also clear, as c becomes smaller the region that can be approximated as 2 dimensional becomes larger. This is explained by considering that $c < 1$ corresponds to scaling two axes of the ellipsoid to become longer, thus creating an oblate spheroid.

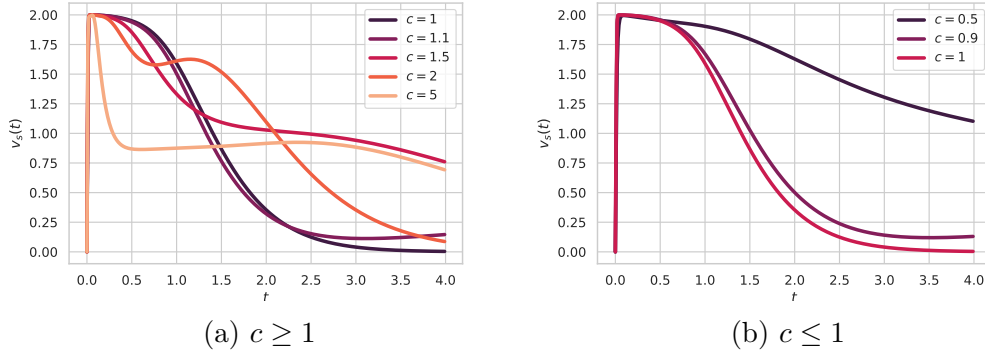


Figure 2: Spectral variance curve of the different deformed spheres.

2.2 Volume

We estimate the volume based on the spectral zeta function as described in [17], of the space.

$$V_{geom} = \frac{(4\pi)^{\frac{d}{2}}}{m} \left(\frac{(\log(\Lambda + 1))^2}{\Lambda} \right)^{\frac{d}{2}} \sum_{\lambda'} \frac{e^{-\lambda'-1}}{\lambda' + 1} \Gamma\left(1 - \frac{d}{2}, 1\right), \quad (19)$$

using rescaled eigenvalues $\lambda' = \frac{(\log(\Lambda+1))^2}{\Lambda} \lambda$. How this volume changes as a function of the deformation parameter c for $n = 20$ is shown in Figure 3, where we have plotted the volume, divided by the volume of the two sphere¹. We see that there is a slight n dependence, but that the value for the round sphere becomes closer to 1 as n increases, marking this n dependence as a cut-off effect. This is an effect of the way the fuzzy sphere is normalized, whereby an increase in n leads to an improved resolution of the geometry, instead of a larger surface. In principle one could change the normalization and generate spheres that keep the resolution fixed, and instead lead to ever larger spheres being described.

3 Implementing visualization for fuzzy spaces

In our past work [1], we implemented code to visualize the truncated spectral triple for a continuum sphere. This code worked by generating localized

¹To be precise we have divided by twice the volume of the two sphere, since the eigenvalue doubling leads to the volume of two spheres appearing here.

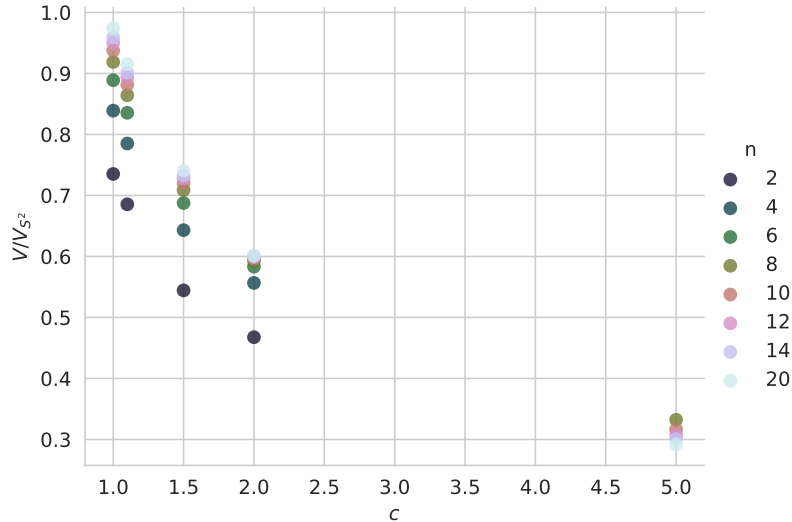


Figure 3: This plot shows the change in the volume of the geometry against the deformation parameter c , for different matrix sizes n .

states, that is states with a small dispersion (defined below in (20)). We were able to show that, for truncated spectral triples, these states converge to points in the infinite matrix size limit. Calculating the Connes distance between these states leads to a distance matrix which was then used to calculate an embedding for the points using a weighted SMACOF algorithm² for stress majorization.

In the following we will explain how this code works, and at the same time elaborate those points of the code that need to be modified to generalize this code to fuzzy spaces in general, and the deformed fuzzy sphere in particular. This covers three points in particular³:

- We require proxies for the coordinates to be able to calculate the dispersion, and generate localized states that are roughly evenly distributed on our geometry.
- We need to determine the number of points we want to generate, this

²SMACOF stands for “Scaling by MAjorizing a COmplicated Function”.

³For the most general fuzzy spaces we would also need to consider how to choose the dimension of the space the geometry is embedded in, however for the deformed fuzzy sphere this will be fixed at $d = 3$, and so we do not discuss it here.

will depend on the cut-off of the geometry, the volume of the geometry and the dimension of the fuzzy space.

- After generating the states we will calculate the Connes distance between them. To do this we require a basis for the algebra to optimize over.

We will cover these problems in the following subsections. The code for the deformed fuzzy sphere visualization, where we implemented these changes, is available under [18].

3.1 The proxies for the coordinate calculation

The first step in visualizing a spectral triple is to generate states of low dispersion, which we showed can, in the context of truncated spectral triples, be understood as well localized. The dispersion for a state s is defined as

$$\delta(s) = \sup_{a \in \mathcal{A}} \left\{ |s(a^2) - s(a)^2| \mid |[D, a]| \leq 1 \right\} . \quad (20)$$

While this is a good definition for a given state, using it in code that tries to find states of minimal dispersion leads to a convex double optimization; we optimize s to minimize $\delta(s)$, but at the same time each $\delta(s)$ optimizes a to maximize it. This type of problem is notoriously hard to solve numerically. It is thus necessary to use a proxy, we used the projector P , which arises from the Heisenberg relation defined in [19]. This gives rise to coordinate matrices $\{X, Y, Z\}$ that give us an approximation of the dispersion

$$\tilde{\delta}(s) = \left\{ \left| \sum_{W \in \{X, Y, Z\}} s(W^2) - s(W)^2 \right| \right\} . \quad (21)$$

We were able to show that, while δ and $\tilde{\delta}$ do not need to be numerically close, they will show the same behaviour, and in particular minimize on similar states, at least for the case of truncated geometries and the limit of large truncations.

Minimizing the dispersion leads to a state that is well localized, however generating an ensemble of points that only minimize the dispersion will lead to points that cluster together, due to the computer algorithm. To cover the entire sphere we added a repulsive potential between the states. We then minimize the dispersion proxy $\tilde{\delta}$ plus a Coulomb potential

$$E(s) = \tilde{\delta}(s) + \sum_i \frac{g}{\tilde{d}(s_i, s)} \quad (22)$$

where the sum goes over all states already generated, and the distance proxy \tilde{d} is

$$\tilde{d}(s_i, s_j) = \left\{ \left| \sum_{W \in \{X, Y, Z\}} s_i(W) - s_j(W) \right| \right\}. \quad (23)$$

We use the distance proxy instead of the Connes distance defined in (1), since this would also lead to a double optimization problem. Again we were able to show that this is a good proxy for the distance, for the truncated spectral triples. We can then generate a set of points by successively minimizing $E(s)$ a set number of times.

For fuzzy spaces the matrices $\{X, Y, Z\}$ can be approximated through the matrices L_i arising in the Dirac operator. This is supported by other work on visualizing fuzzy spaces (without the entire machinery of the spectral triple attached) in [20]. It is also the simplest solution, since these matrices are the only data available to us, without adding additional input into our system. For the present article we thus effectively use

$$\tilde{\delta}(s) = \left\{ \left| \sum_i s(L_i^2) - s(L_i)^2 \right| \right\} \quad (24)$$

$$\tilde{d}(s_1, s) = \left\{ \left| \sum_i s_1(L_i) - s(L_i) \right| \right\}. \quad (25)$$

3.2 The number of points and dimension

The number of points that can be generated depends on the resolution of the truncated space or the matrix size of the finite spectral triple. Our code determines the number of localized states to search, based on the dispersion of the states obtained δ , and the overall volume of the space V_{geom} . The maximal number of states we generate is given as $V_{geom}/(\delta^d B_d)$, where B_d is the volume of unit sphere in d dimension. To calculate this we need to estimate the dimension, for which we use the spectral dimension as described in [6], and the volume as already discussed above in (19)

To estimate the dimension of the geometry we evaluate the spectral dimension at the point $t_d = \frac{(\log(\Lambda+1))^2}{\Lambda}$, where Λ is the largest absolute value among the eigenvalues. This value is chosen based on [17] to lie above the region where the finite size of the matrices starts to influence the result, but well below the region where the large scale structure of the geometry will

start to interfere. Since this does not necessarily lead to an integer value for the dimension, we round the result to the closest integer.

The other ingredient to estimate the number of states is the dispersion δ of the states. In [1] this was estimated based on the eigenvalue cut-off of the geometry as $\log(\Lambda_{cutoff})/\Lambda_{cutoff}^2$. While this works well for truncated continuum geometries it does not generalize to fuzzy spaces. A more universal (and precise) way to approximate the maximal number of non-overlapping states for the geometry is to use the dispersion δ of the generated states from the code. The behaviour of this dispersion as a function of the matrix size n is illustrated in Figure 4a. The dispersion of the states is independent of the deformation, since the algebra of generators is the same for all deformation parameters.

So we find that the dispersion of the states depends on n , but not on the deformation of the geometry, while the volume, as we saw above, is almost independent of n , but strongly changes with the deformation. The dimension of the geometry is stable at 2, except for geometries with very low matrix size, where the resolution of the geometry is not sufficient to show the 2d dimensional nature of the deformed sphere. We exclude these in our plot of the number of expected states, which we show in Figure 4b. Comparing it to Figure 3 above we can see that the change of the volume with c is what drives the change in the maximal number of states.

This image clearly shows that the number of states rises linearly with n , which, from our equation to calculate the maximal number of states, implies that the dispersion of the states falls off like n^{-2} . Unfortunately the computational complexity per state rises fast. A test run showed that the generation of two states and evaluation of their distance scales strongly with n^4 , and the number of pairs whose distance needs to be evaluated scales like n^2 . So even though the number of states does not rise quickly, the time to calculate them does, thus limiting us in the size of matrices we can use. However, as we will show below even for $n = 8$ the algebra contains enough information to lead to impressive visualizations of the geometries.

⁴A short exploratory run was not able to determine whether it scales like a higher power law, or exponentially.

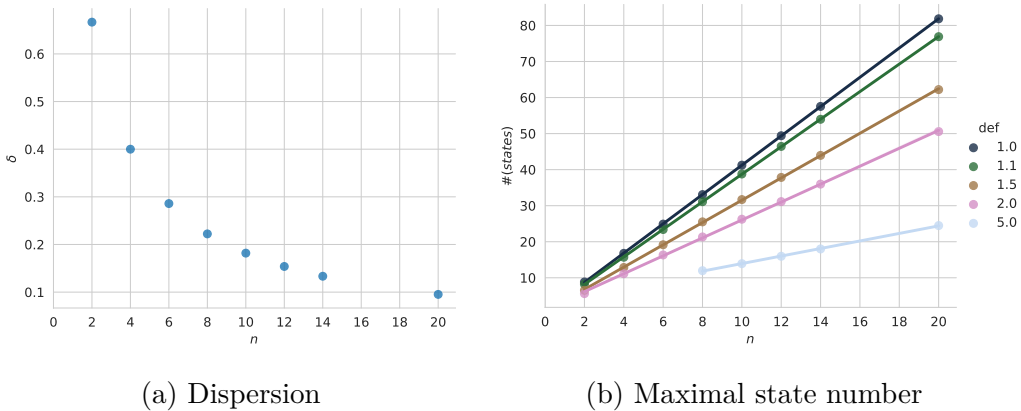


Figure 4: The left-hand plot shows the change in the dispersion with n . The right-hand image shows the estimated number of states as a function of n . The colour indicates the deformation parameter used, clearly each deformation has a different linear dependence.

3.3 Choosing a basis for the algebra

After having generated the states, we need to calculate their distance, using the Connes distance function. Since the states are fixed at this point we can optimize the exact expression, to do this we use a basis of the algebra \mathcal{A} . For the truncated sphere the natural basis of the algebra is formed by a truncated matrix representation of the spherical harmonics, which we used in our past work [1] to calculate the Connes distance between states.

In the case of the deformed sphere we are not given a basis a priori, however we are handed the generators of the algebra, in the form of the algebra elements L_i that are part of the Dirac operator.

We then generate a basis for the space of all algebra elements by calculating all products of the L_i , applying the Poincaré-Birkhoff-Witt theorem. Since the L_i for the deformed sphere satisfy the usual commutation relations we can use this to reduce the number of states to calculate. We also check each generated element and do not keep it if it is linearly dependent on any already generated element.

For more general finite spectral triples this will not generally be true. However, it is possible to choose the most naive basis on $M_n(\mathbb{C})$, using all matrices with only one non-zero entry, and find comparable results. This choice of algebra is also implemented as an option in our code.

4 Images of a deformed fuzzy sphere

To test the code we generated embeddings of deformed fuzzy spheres. We will first discuss the constrained case with c_0, c_{12}, c_{13} at 1 and $c_{23} = c$ at the end of the section observe some more general deformations. The results would be equivalent if we had changed one of the other two directions and kept this one constant. The embedding for these deformed fuzzy spheres for $n = 8$ are shown in Figures 5 and 6.

To understand these images better we have fit ellipsoids to the embedding data. These fits have five degrees of freedom, two angles of rotation for the main axis⁵, and the three deformation parameters a_k . Since we fit the three deformation parameters, the radius can be held fixed at 1, as a change in radius is simply a simultaneous rescaling of all axes by the same amount. For the fit we optimized a function f which was the sum of the square of the differences from each point to the fitted ellipsoid, and the fit itself done via python's optimize library [21].

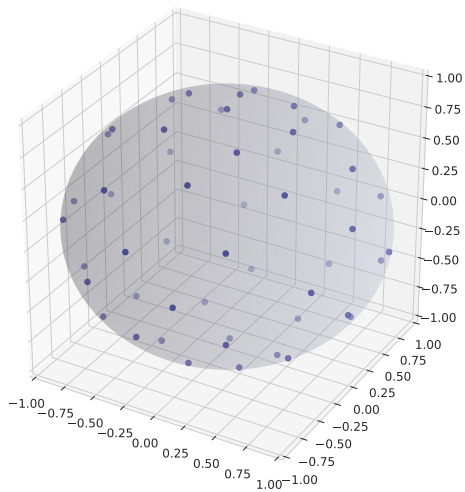
In Table 1 we compare the results for these fits with our expected deformations from equation (16). We find that they do agree reasonably well, taking into account that, especially for $c_{13} = 5$ we are fitting 5 free parameters to 11 points. The fits for the rounder states, where more points are available are thus better.

The data works equally well for $c < 1$ as for $c > 1$ which was to be expected. The difference between $c < 1$ and $c > 1$ is that the former leads to oblate spheroids, while the latter leads to prolate spheroids.

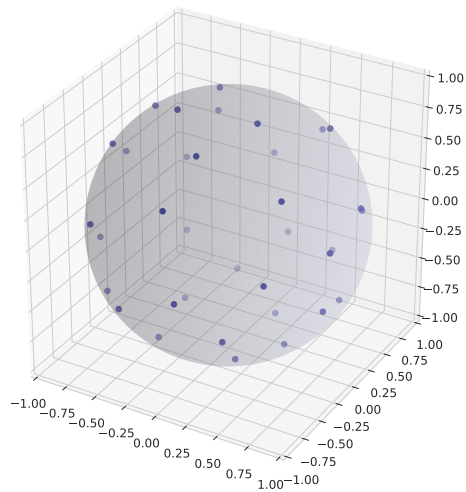
4.1 Correlation coefficient

Another tool to check our visualization, is to compare how well the distance between the states in the embedding agrees with the distance of the points calculated according to the spectral distance. The easiest way to do so, is to observe the correlation coefficient between these two quantities. If the constellation of points does not embed into the flat space provided for the embedding the algorithm will try to do its best, but will not be able to embed all points well, and thus the correlation coefficient will be high for some points. As an example for this we have run an embedding of the fuzzy S^2 into 2d space.

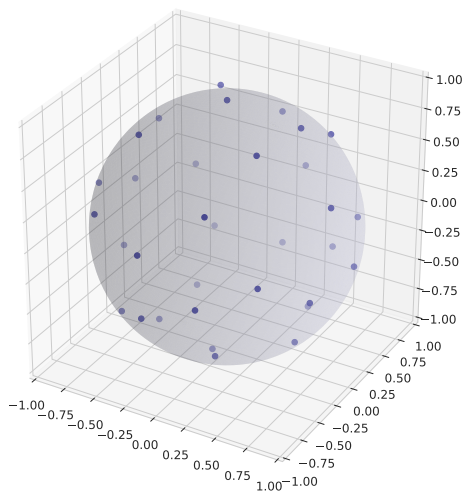
⁵Since the embedding algorithm starts with a random point, the direction of the embedding is random.



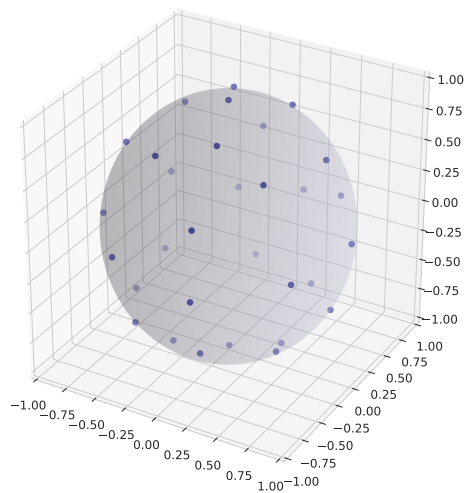
(a) $c = 0.5$



(b) $c = 0.9$



(c) $c = 1.0$



(d) $c = 1.1$

Figure 5: Embeddings of the deformed spheres with their best fit ellipsoids plotted for comparison.

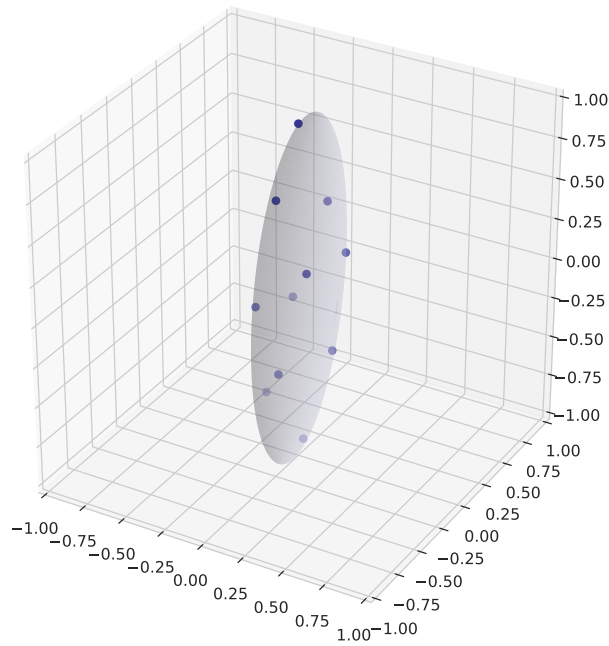
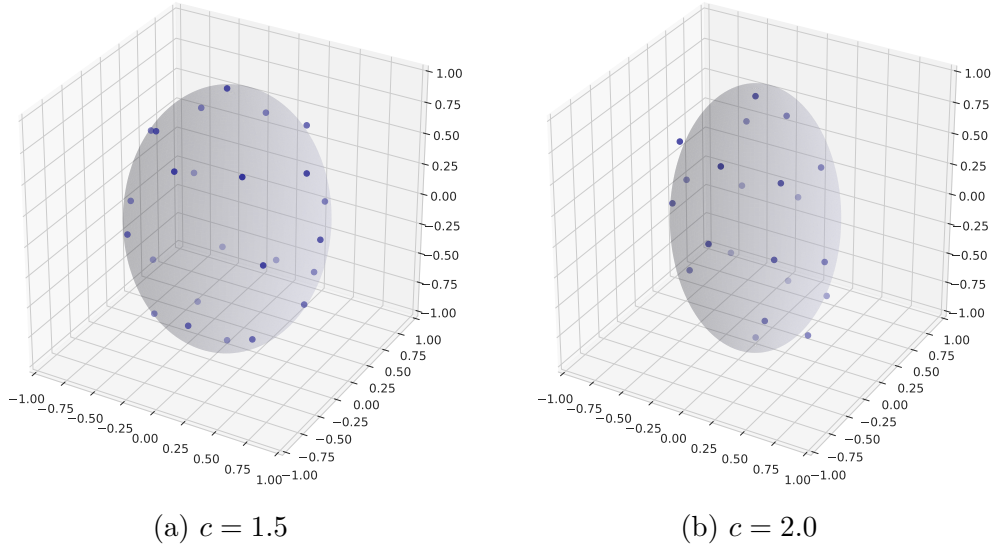


Figure 6: Embeddings of the deformed spheres with their best fit ellipsoids plotted for comparison.

Table 1: Best fit values for the main axes of the ellipses.

c	expected axes	best fit axes	angle of axis	f / d.o.f.
0.50	(1.00, 2.00, 2.00)	(0.96, 1.18, 1.19)	(0.00, 3.14)	0.0020
0.90	(1.00, 1.11, 1.11)	(1.00, 1.01, 1.03)	(-0.00, 0.83)	0.0024
1.00	(1.00, 1.00, 1.00)	(0.98, 0.99, 0.99)	(0.39, 0.00)	0.0015
1.10	(0.91, 0.91, 1.00)	(0.92, 0.93, 1.01)	(0.01, 0.39)	0.0008
1.50	(0.67, 0.67, 1.00)	(0.73, 0.75, 1.03)	(0.03, 0.21)	0.0025
2.00	(0.50, 0.50, 1.00)	(0.58, 0.61, 1.06)	(-0.00, 0.59)	0.0224
5.00	(0.20, 0.20, 1.00)	(0.24, 0.25, 1.13)	(1.67, -0.00)	0.0358

In the left-hand image of Figure 7 we show the scatter of the value of the correlation coefficient, which in this example ranges from 0.3 to 1. It is clear that while the algorithm is able to match the distances well for some points, it eventually finds points that can not be reconciled with all the others, leading to low values. In the right-hand image we plot the 2d embedding, and colour the points by their correlation coefficient. It is then clear that the points that lie in the middle of the circle do not embed well.

In Figure 8 we show the correlation coefficients for the embedding into 3d. Here the diamond shape marks the average value for a given c , while the transparent points in the background show the values for each individual point, and thus illustrate that there is little spread.

4.2 Distance histograms

The correlation coefficient reduces the data to one convenient number, however it only tells us how well the embedding reproduces the distances we have calculated. What we would like to do is find some more quantities to, at least qualitatively, compare how well the geometry we find agrees with an ellipsoid. One such quantity is the collection of the distances between all pairs of points, which can be plotted as a histogram.

This is also sensitive to the question whether the Connes distance measure finds the Euclidean distance in the embedding space, or the distance along the sphere. In Figure 9 we show the distance distribution for the round $c = 1$ case, compared to the distance distribution of evenly distributed points for a sphere calculated using the Euclidean distance on \mathbb{R}^3 or the distance on the sphere.

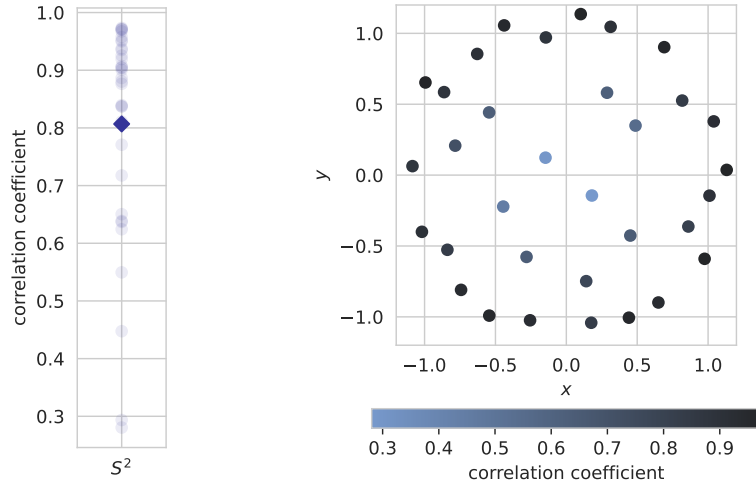


Figure 7: To demonstrate the correlation coefficient for a failed embedding we have here embedded the fuzzy S^2 without deformation into 2d. While the right-hand image of the embedding seems reasonable, the left-hand image of the correlation coefficients shows us that this embedding did not work well.

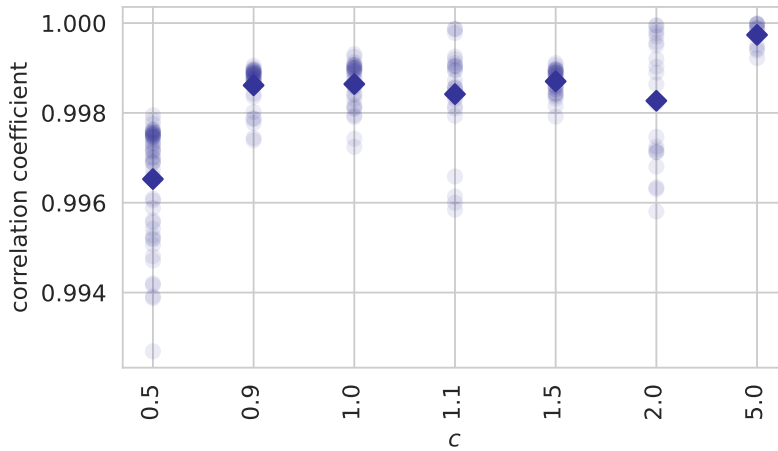


Figure 8: Correlation between the distances in the embedding and the distance between the states. The diamond marks the average value, while the transparent points show the values for each individual point.

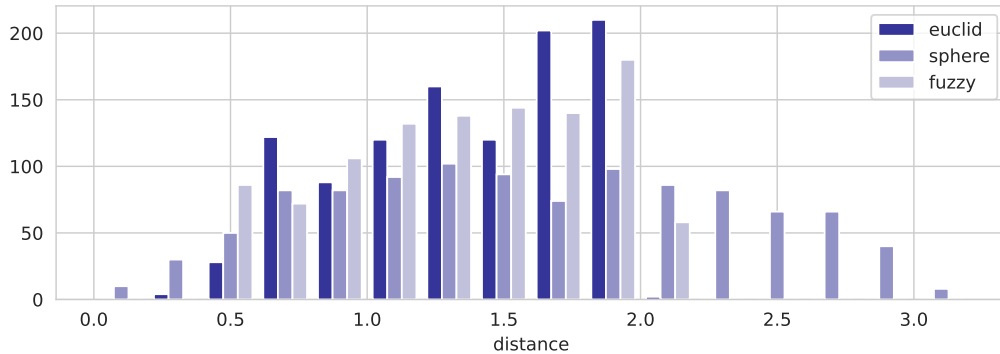


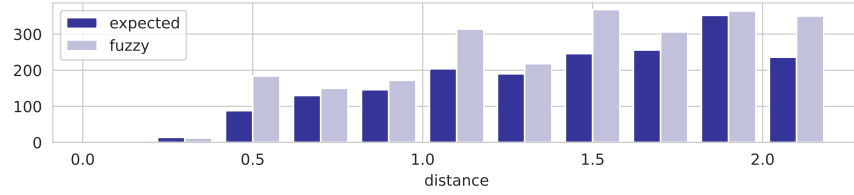
Figure 9: Histogram of the distance between points for the round sphere, comparing the distances found using the Euclidean distance measure, as well as those measured along the sphere with those found from the Connes distance for our embedded fuzzy spaces.

This figure shows clearly that the Connes distance reproduces the Euclidean distance between points and not the distance on the sphere. To ponder why this might be the case we go back to the construction for the Dirac operator in [22]. The construction for the Dirac operator for the fuzzy sphere does use the 3 dimensional embedding space of the two sphere, which is restricted to the surface of the sphere by fixing the radius. It then seems that Connes distance function on the finite spectral triple does not only include points on the surface of the sphere, but also those in the embedding geometry. This question deserves some further study.

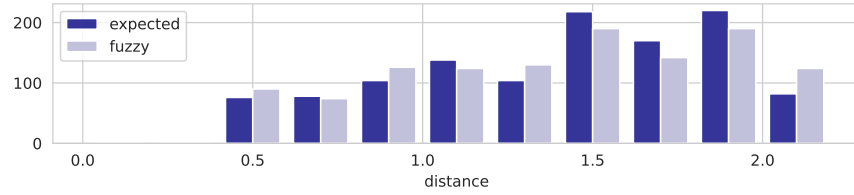
To compare our data for the deformed sphere we can take a sampling of points on an ellipsoid, which was achieved by minimizing a repulsive potential, to generate a random but uniform distribution of points, similar to what we expect to find from our sampling algorithm for the fuzzy space. As explained above we use an ellipsoid with one axis of length 1 and two axes rescaled to $1/c$.

The results are shown in Figures 10 and 11 with the data for the fuzzy space embeddings in light blue and the data generated from a continuum embedding in dark blue. The histograms for the two samples agree well, within the limitation of the small sample size. Since generating each embedding takes several days it is not practical to generate more for sampling purposes.

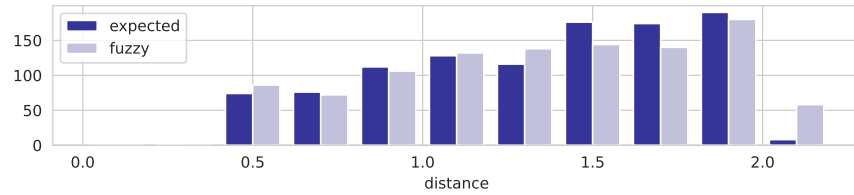
We thus conclude that this observable is also well compatible with the



(a) $c = 0.5, N = 52$

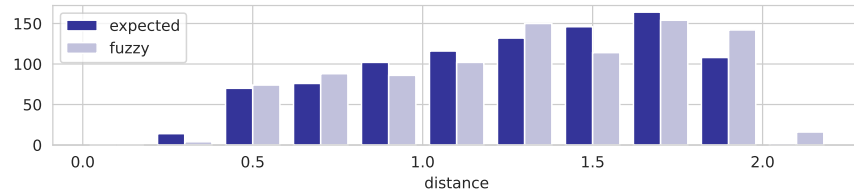


(b) $c = 0.9, N = 35$

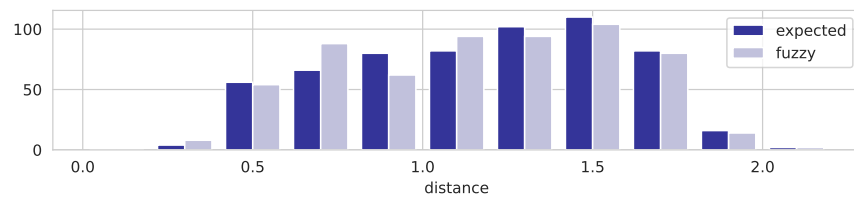


(c) $c = 1, N = 33$

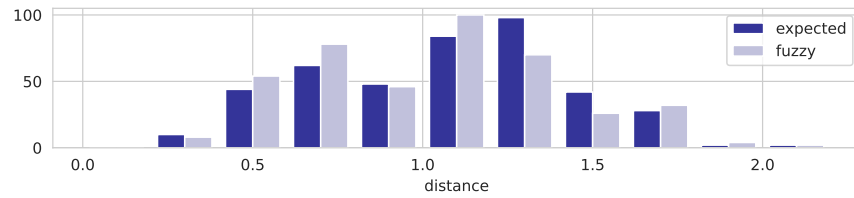
Figure 10: Histogram of the distances for $n = 8$, for $c = 0.5, 0.9, 1.0$. The histograms generated from spheroids are dark blue, while the histogram for the fuzzy spaces is light blue. The number of states N is given for each, since we generated as many points for each expected state as we found in the corresponding simulation.



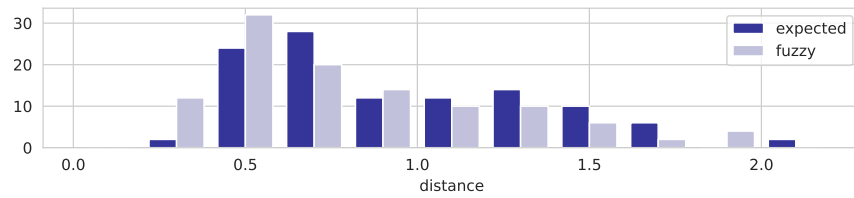
(a) $c = 1.1, N = 31$



(b) $c = 1.5, N = 25$



(c) $c = 2.0, N = 21$



(d) $c = 5.0, N = 11$

Figure 11: Histogram of the distances for $n = 8$, for $c = 1.1, 1.5, 2.0, 5.0$. The histograms generated from spheroids are dark blue, while the histogram for the fuzzy spaces is light blue. The number of states N is given for each, since we generated as many points for each expected state as we found in the corresponding simulation.

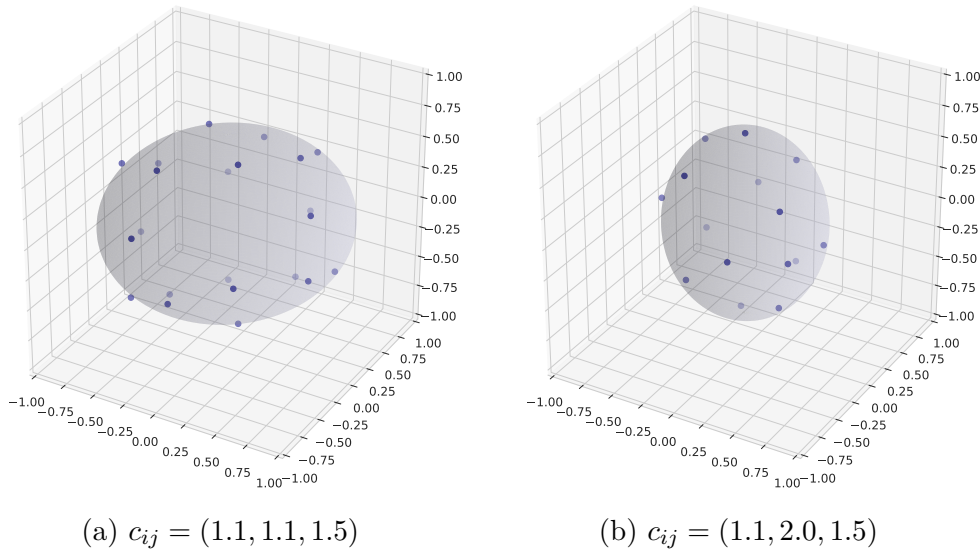


Figure 12: Two examples of more general deformed spheres.

expectation that our deformed fuzzy space is an ellipsoid.

4.3 A more general deformed sphere

While we do not have an analytic equation for the eigenvalues of the Dirac operator with general deformations, our code can easily deal with arbitrary values of the c_{ij} ⁶.

We have thus tested this, again for $n = 8$ and fit the data with ellipsoids as explained above. In Figure 12 we show this for the two cases of $c_{ij} = (1.1, 1.1, 1.5)$ and $c_{ij} = (1.1, 2.0, 1.5)$. The fit data for all states generated is given in the appendix in table 2. While these fits overall work well, there are several outliers where the algorithm was not able to find a good fit. This is likely partly due to fact that the deformation leads to smaller volumes, and thus fewer states, which means less data to constrain the fit. Running a less constrained fit on the computer leaves more opportunities to find fits that minimize the function, but are not actually the ‘true’ hidden geometry.

So while our analytic understanding of the eigenvalues is restricted to the simpler case, our code can generate embeddings for the more complicated

⁶ c_0 is fixed to 1 however an overall rescaling of D can always set this to 1.

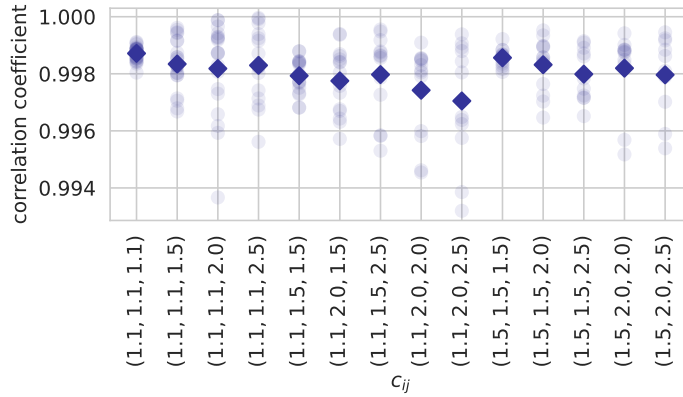


Figure 13: Correlation coefficient for the fuzzy sphere when it is deformed in several directions.

class of deformed fuzzy spheres, and they can still be fit through ellipsoids. It thus seems that our qualitative understanding of the geometry works well. In Figure 13 we show the correlation coefficient between the distances of the points in the embedding and those found using the spectral distances for the multiply deformed sphere. As for the case with deformation in only a single direction the correlation coefficient is extremely close to 1, leading us to believe that the multi deformed sphere also works well.

5 Conclusion and outlook

In this article we have studied the Dirac operator for a deformed fuzzy sphere. We found that, simply rescaling the terms in the Dirac operator for the fuzzy sphere does lead to a geometry that can be described as an ellipsoid. We studied some spectral observables for the deformed fuzzy sphere, among them examining the spectral variance of the object.

Next we used this new geometry as a test case in generalizing the algorithm proposed in [1] from truncated spectral triples to finite spectral triples, sometimes also called fuzzy spaces. We were able to obtain visualizations of the deformed fuzzy sphere, which agreed well with the expectation. Fitting the length of the axes of the embedded geometries led to values close to the expected values, within the uncertainties arising from single instance numerical work.

Another method to test the veracity of the embedding was to study the correlation between the distances as embedded, and the distances calculated. This measures if the geometries can actually be embedded in flat 3 dimensional space. The correlation coefficients all came out extremely close to 1 confirming that the geometries embed well.

This work is a first step into visualizing finite spectral triples. A promising next step would be to visualize the fuzzy torus [23]. One particularly interesting property of the torus in this context is that it can only embed into 2 or 4 dimensions, it would thus be fascinating to see how trying to embed it into the ‘wrong’ dimension changes the results, and to compare its embedding in these two cases.

This would of course only be first steps towards a general purpose code to generate images of any finite spectral triple one might write down. This code would then be very useful in trying to understand the results arising from the research program into random finite spectral triples.

The code used to generate the visualizations of the deformed fuzzy sphere is available on GitHub [18]. The full set of data generated for this article is also available for download, together with some scripts to start exploring them, in the encyclopedia of quantum geometries [24].

Acknowledgements

I am grateful to Abel Stern, for continuing discussions about this project, even though he has left academia. I have also had great discussions helping to understand the spectrum with John Barrett and Thomas Laird. I’d also like to thank the Erwin Schrödinger Institute in Vienna, where John and Thomas were visiting during some of these discussions.

References

- [1] L. Glaser and A. B. Stern. ‘Reconstructing manifolds from truncations of spectral triples’. In: *Journal of Geometry and Physics* 159 (2021), p. 103921. ISSN: 0393-0440. DOI: <https://doi.org/10.1016/j.geomphys.2020.103921>.

- [2] J. W. Barrett and L. Glaser. ‘Monte Carlo simulations of random non-commutative geometries’. In: *J.Phys.* A49 (May 2016), p. 245001. DOI: 10.1088/1751-8113/49/24/245001.
- [3] A. Connes. *Noncommutative Geometry*. English. San Diego: Academic Press, Dec. 1994. ISBN: 978-0-12-185860-5.
- [4] J. W. Barrett. ‘Matrix geometries and fuzzy spaces as finite spectral triples’. In: *Journal of Mathematical Physics* 56.8 (Aug. 2015), p. 082301. ISSN: 0022-2488, 1089-7658. DOI: 10.1063/1.4927224.
- [5] L. Glaser. ‘Scaling behaviour in random non-commutative geometries’. en. In: *Journal of Physics A: Mathematical and Theoretical* 50.27 (2017), p. 275201. ISSN: 1751-8121. DOI: 10.1088/1751-8121/aa7424.
- [6] J. W. Barrett, P. Druce and L. Glaser. ‘Spectral estimators for finite non-commutative geometries’. en. In: *Journal of Physics A: Mathematical and Theoretical* 52.27 (June 2019), p. 275203. ISSN: 1751-8121. DOI: 10.1088/1751-8121/ab22f8.
- [7] M. D’Arcangelo. ‘Numerical Simulation of Random Dirac Operators’. PhD thesis. Nottingham: University of Nottingham, 2022.
- [8] S. Azarfar and M. Khalkhali. ‘Random Finite Noncommutative Geometries and Topological Recursion’. In: *arXiv:1906.09362 [hep-th, physics:math-ph]* (June 2019). arXiv: 1906.09362. URL: <http://arxiv.org/abs/1906.09362>.
- [9] M. Khalkhali and N. Pagliaroli. ‘Phase Transition in Random Noncommutative Geometries’. In: *arXiv:2006.02891 [hep-th, physics:math-ph]* (Dec. 2020). arXiv: 2006.02891. DOI: 10.1088/1751-8121/abd190. URL: <http://arxiv.org/abs/2006.02891>.
- [10] H. Hessam, M. Khalkhali and N. Pagliaroli. ‘Bootstrapping Dirac Ensembles’. In: *arXiv:2107.10333 [hep-th, physics:math-ph]* (July 2021). arXiv: 2107.10333. URL: <http://arxiv.org/abs/2107.10333>.
- [11] C. I. Pérez-Sánchez. ‘On Multimatrix Models Motivated by Random Noncommutative Geometry I: The Functional Renormalization Group as a Flow in the Free Algebra’. en. In: *Annales Henri Poincaré* 22.9 (Sept. 2021), pp. 3095–3148. ISSN: 1424-0661. DOI: 10.1007/s00023-021-01025-4.

- [12] M. Khalkhali and N. Pagliaroli. ‘Spectral Statistics of Dirac Ensembles’. In: *arXiv:2109.12741 [hep-th, physics:math-ph]* (Sept. 2021). arXiv: 2109.12741. URL: <http://arxiv.org/abs/2109.12741>.
- [13] H. Hessam, M. Khalkhali and N. Pagliaroli. ‘Double scaling limits of Dirac ensembles and Liouville quantum gravity’. In: *J. Phys. A* 56.22 (2023), p. 225201. DOI: 10.1088/1751-8121/acfd6.
- [14] L. Verhoeven. ‘Geometry in spectral triples: Immersions and fermionic fuzzy geometries’. In: *Electronic Thesis and Dissertation Repository* (Aug. 2023). URL: <https://ir.lib.uwo.ca/etd/9561>.
- [15] J. W. Barrett and L. Glaser. ‘Work in progress’. In: ()
- [16] J. Ambjørn, J. Jurkiewicz and R. Loll. ‘The Spectral Dimension of the Universe is Scale Dependent’. In: *Physical Review Letters* 95.17 (Oct. 2005), p. 171301. DOI: 10.1103/PhysRevLett.95.171301.
- [17] A. B. Stern. ‘Finite-rank approximations of spectral zeta residues’. en. In: *Letters in Mathematical Physics* (July 2018). ISSN: 1573-0530. DOI: 10.1007/s11005-018-1117-5. URL: <https://doi.org/10.1007/s11005-018-1117-5>.
- [18] L. Glaser. *Deformed fuzzy sphere visualisation*. https://github.com/LisaGlaser/deformed_sphere_visualisation. 2023.
- [19] A. H. Chamseddine, A. Connes and V. Mukhanov. ‘Geometry and the Quantum: Basics’. In: *Journal of High Energy Physics* 2014.12 (Dec. 2014). arXiv: 1411.0977. ISSN: 1029-8479. DOI: 10.1007/JHEP12(2014)098. URL: <http://arxiv.org/abs/1411.0977>.
- [20] L. Schneiderbauer and H. C. Steinacker. ‘Measuring finite Quantum Geometries via Quasi-Coherent States’. In: *Journal of Physics A: Mathematical and Theoretical* 49.28 (July 2016). arXiv: 1601.08007, p. 285301. ISSN: 1751-8113, 1751-8121. DOI: 10.1088/1751-8113/49/28/285301.
- [21] P. Virtanen et al. ‘SciPy 1.0: Fundamental Algorithms for Scientific Computing in Python’. In: *Nature Methods* 17 (2020), pp. 261–272. DOI: 10.1038/s41592-019-0686-2.
- [22] H. Grosse and P. Prešnajder. ‘The dirac operator on the fuzzy sphere’. en. In: *Letters in Mathematical Physics* 33.2 (), pp. 171–181. ISSN: 0377-9017, 1573-0530. DOI: 10.1007/BF00739805.

- [23] J. W. Barrett and J. Gaunt. ‘Finite spectral triples for the fuzzy torus’. In: (Aug. 2019). arXiv: 1908.06796 [math.QA].
- [24] L. Glaser. *Deformed fuzzy spheres*. Version v2. Zenodo, Apr. 2023. DOI: 10.5281/zenodo.7864066. URL: <https://doi.org/10.5281/zenodo.7864066>.

A General deformed sphere

Table 2: Fit data for general deformed spheres.

c_{ij}	expected axes	best fit axes	angle of axis	$f/$ d.o.f.
(1.10, 1.10, 1.10)	(0.83, 0.83, 0.83)	(0.89, 0.90, 0.91)	(0.60, 0.00)	0.0036
(1.10, 1.10, 1.50)	(0.61, 0.61, 0.83)	(0.72, 0.72, 0.93)	(0.01, 0.70)	0.0013
(1.10, 1.10, 2.00)	(0.45, 0.45, 0.83)	(0.56, 0.57, 0.97)	(0.34, -0.00)	0.0087
(1.10, 1.10, 2.50)	(0.36, 0.36, 0.83)	(0.47, 0.59, 0.96)	(0.00, 0.00)	0.1137
(1.10, 1.50, 1.50)	(0.44, 0.61, 0.61)	(0.67, 0.73, 0.73)	(-0.00, 0.71)	0.0024
(1.10, 1.50, 2.50)	(0.27, 0.36, 0.61)	(0.44, 0.49, 0.76)	(0.82, 1.58)	0.0315
(1.10, 1.50, 2.00)	(0.33, 0.45, 0.61)	(0.54, 0.57, 0.77)	(0.40, 0.38)	0.0125
(1.10, 2.00, 2.00)	(0.25, 0.45, 0.45)	(0.49, 0.58, 0.59)	(0.07, -0.00)	0.0101
(1.10, 2.00, 2.50)	(0.20, 0.36, 0.45)	(0.43, 0.48, 0.58)	(0.89, 1.64)	0.0249
(1.50, 1.50, 1.50)	(0.44, 0.44, 0.44)	(0.66, 0.66, 0.66)	(0.01, 0.00)	0.0090
(1.50, 1.50, 2.00)	(0.33, 0.33, 0.44)	(0.54, 0.54, 0.68)	(0.25, 1.55)	0.0144
(1.50, 1.50, 2.50)	(0.27, 0.27, 0.44)	(0.46, 0.47, 0.64)	(0.11, 0.16)	0.0229
(1.50, 2.00, 2.00)	(0.25, 0.33, 0.33)	(0.49, 0.55, 0.56)	(0.00, 0.30)	0.0342
(1.50, 2.00, 2.50)	(0.20, 0.27, 0.33)	(0.43, 0.52, 0.53)	(0.00, 0.00)	0.0458